

Experimental demonstration of influence of underwater turbulence on ghost imaging

Man-Qian Yin(殷曼倩), Le Wang(王乐), Sheng-Mei Zhao(赵生妹)
Citation: Chin. Phys. B . 2019, 28(9): 094201 . **doi:** 10.1088/1674-1056/28/9/094201
Journal homepage: http://cpb.iphy.ac.cn; http://iopscience.iop.org/cpb

What follows is a list of articles you may be interested in

Mask-based denoising scheme for ghost imaging

Yang Zhou(周阳), Shu-Xu Guo(郭树旭), Fei Zhong(钟菲), Tian Zhang(张天)
Chin. Phys. B . 2019, 28(8): 084204 . **doi:** 10.1088/1674-1056/28/8/084204

Analysis of melt ejection during long pulsed laser drilling

Ting-Zhong Zhang(张廷忠), Zhi-Chao Jia(贾志超), Hai-Chao Cui(崔海超), De-Hua Zhu(朱德华), Xiao-Wu Ni(倪晓武), Jian Lu(陆健)
Chin. Phys. B . 2016, 25(5): 054206 . **doi:** 10.1088/1674-1056/25/5/054206

Image encryption using random sequence generated from generalized information domain

Xia-Yan Zhang(张夏衍), Guo-Ji Zhang(张国基), Xuan Li(李璇), Ya-Zhou Ren(任亚洲), Jie-Hua Wu(伍杰华)
Chin. Phys. B . 2016, 25(5): 054201 . **doi:** 10.1088/1674-1056/25/5/054201

Lensless ghost imaging through the strongly scattering medium

Zhe Yang(杨哲), Lianjie Zhao(赵连洁), Xueliang Zhao(赵学亮), Wei Qin(秦伟), Junlin Li(李俊林)
Chin. Phys. B . 2016, 25(2): 024202 . **doi:** 10.1088/1674-1056/25/2/024202

Increasing the range accuracy of three-dimensional ghost imaging ladar using optimum slicing number method

Yang Xu, Zhang Yong, Xu Lu, Yang Cheng-Hua, Wang Qiang, Liu Yue-Hao, Zhao Yuan
Chin. Phys. B . 2015, 24(12): 124202 . **doi:** 10.1088/1674-1056/24/12/124202

Experimental demonstration of influence of underwater turbulence on ghost imaging*

Man-Qian Yin(殷曼倩)†, Le Wang(王乐)†, and Sheng-Mei Zhao(赵生妹)‡

Institute of Signal Processing and Transmission, Nanjing University of Posts and Telecommunications, Nanjing 210003, *China*

(Received 16 May 2019; revised manuscript received 20 June 2019; published online 20 August 2019)

It is difficult to obtain a clear image in underwater turbulence environment with classical imaging methods due to the absorption, scattering, and underwater turbulence on the propagation beam. However, ghost imaging (GI), a non-locally imaging technique, has shown the turbulence-free ability in atmospheric turbulence by exploiting the second-order correlation between the signal beam and the reference beam. In this paper, we experimentally investigate the imaging quality of GI affected by the underwater environment, where the underwater environment is simulated by a 1 m×0.4 m×0.4 m tank with distilled water. The water temperature is controlled by a heater inside the tank, and a temperature gradient is obtained by putting the heater at different positions of the tank. The water vibration is produced by a heavy force, and the turbid medium is obtained by dissolving very small specks of $CaCO_3$ in the water. A set of Hadamard speckle pattern pairs are generated and modulated on the incident beam, and then the beam illuminates on an unknown object after passing through the simulated underwater environment. With the second-order correlations, the image is reconstructed under different temperature gradients, water vibration, and turbid medium ratios. The results show that GI has the turbulence-free ability under lower temperature gradient, water vibration, and turbid media. The structural similarity image measurement (SSIM) values of the reconstructed images only start to decrease when the temperature gradient is greater than 4.0 °C. The same temperature gradient produced at the different positions has a little effect on the quality of the underwater GI.

Keywords: underwater ghost imaging, temperature gradient, turbid media, water vibration

PACS: 42.30.Va, 42.30.Wb, 42.68.–w, 92.05.Hj **DOI:** 10.1088/1674-1056/ab33ee

1. Introduction

Underwater imaging technology has played an important role in military, marine development, and engineering applications. However, the quality of classical optical imaging is inevitably constrained by absorptive and scattering effects in underwater environment,[1] which becomes a key issue for the long distance underwater imaging. For example, McGlamery and Hou analyzed the turbulence-degraded images by random phases screen simulation and the optical transfer function under oceanic turbulence, respectively.[2,3] The effect of oceanic turbulence on the quality of imaging in natural water was later discussed in Ref. [4].

In a different context, ghost imaging (GI) is one of the hot spots in the field of quantum optics in recent decades,[5,6] which is based on the second-order correlation of the light intensity fluctuations. Normally, there are two beams in a GI system, one is the signal beam, which is received by a bucket detector that does not have spatial resolution. The other is the reference beam, which is received by a point detector with spatial resolution. By intensity correlation between the signal and reference beams, GI could non-locally obtain an image of an unknown object, and has provided a method to obtain a clear image in instance where sometimes the conventional imaging techniques are infeasible.

GI was first experimentally demonstrated by Pittman *et al.* in 1995 based on quantum entanglement.[7] Then, the realization of GI with classical light source (pseudo thermal light) was proposed in 2002 by Bennink *et al.*[8] Thereafter, the mechanism and implementation of GI were discussed.[9–26]

Later, a new configuration of GI, named computational GI (CGI), was presented to simplify the experimental requirements of GI.[10] At the same time, the improved methods, for example, differential ghost imaging,[11] normalized ghost imaging,[12] corresponding ghost imaging,[13,14] compressive sensing ghost imaging,[15–18] and polarization difference ghost imaging method,[19] were proposed to enhance the imaging quality or to reduce the imaging time.

The turbulence-free property of GI in atmosphere turbulence has already been discussed.[27,28] Whether GI has this property in oceanic turbulence? In 2015, Xiang *et al.* discussed the feasibility of underwater GI.[29] Later, the underwater GI through different transparent liquids was studied in Ref. [30]. The computational GI under different underwater turbidities and different angles was investigated in Ref. [31]. The theoretical analysis of GI under oceanic turbulence was presented in Ref. [32]. The image quality affected by oceanic turbulence was studied in Ref. [33], and the underwater ghost

*Project supported by the National Natural Science Foundation of China (Grant Nos. 61871234 and 11847062) and the Natural Science Foundation of Jiangsu Province, China (Grant No. BK20180755).

†These authors contributed equally to this work.

‡Corresponding author. E-mail: zhaosm@njupt.edu.cn

© 2019 Chinese Physical Society and IOP Publishing Ltd

imaging experiment with low light and high visibility was analyzed in Ref. [34].

It is known that temperature fluctuations may introduce the beam's dissipation, vibration can affect the beam's propagation, and the beam wavefront is distorted and scattered by the turbid medium. All these, in principle, will affect the imaging quality of underwater CGI.

In the paper, we experimentally investigated the imaging quality of CGI under different underwater environments, where a 1 m×0.4 m×0.4 m tank with distilled water was used to simulate the underwater environment. The temperature fluctuations were controlled by a heater inside the tank, and the heater was put on different positions of the tank to obtain the effects of temperature gradient. The water vibration was caused by a heavy force. The turbid medium was obtained by dissolving very small specks of $CaCO_3$ in the water. A set of Hadamard speckle pattern pairs were generated and modulated on the incident beam, and then the beam passed through the simulated underwater environment, and illustrated on an unknown object. With the intensity signals detected by the bucket detector, the object image under underwater environment was obtained by the second-order correlations. With different temperature gradients, different heights of the water vibrations, and different quantity ratios of $CaCO_3$ in the water, the impact of them on the underwater computational GI system was analyzed.

The organization of the paper is as follows. The experimental setup of underwater GI is introduced in Section 2. The impact of the temperature gradient, water vibration, and turbidity on CGI is presented in Section 3, and some conclusions are drawn in Section 4.

2. Experimental setup and theoretical analysis

The experimental setup of the underwater CGI system is shown in Fig. 1.

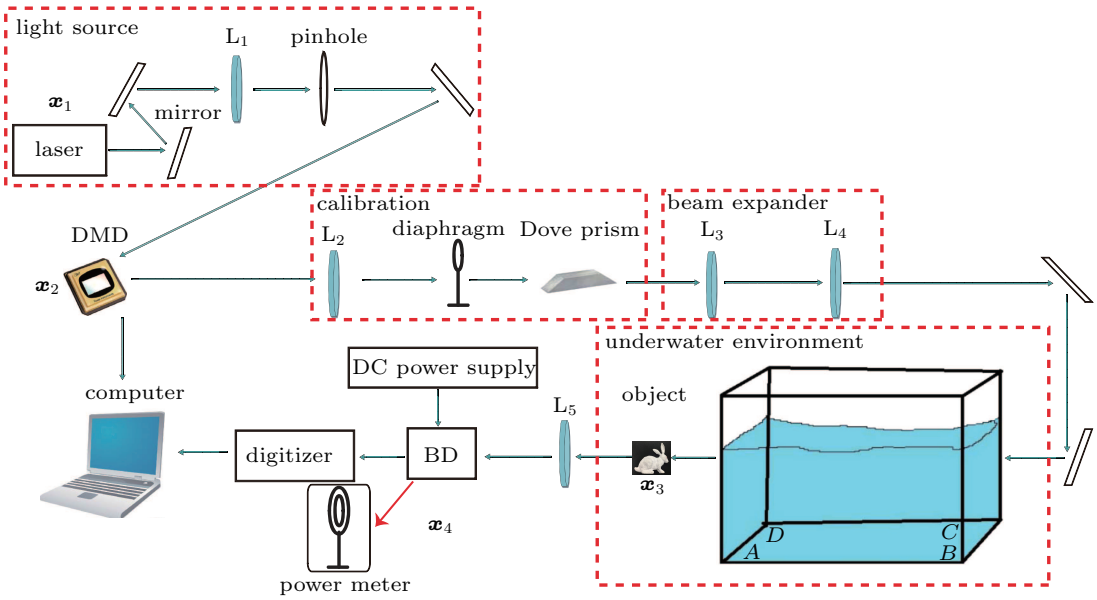


Fig. 1. Experimental setup of CGI under underwater environment.

The laser (LDM405) with $\lambda = 405$ nm and $P = 4$ mW was used to produce the beam. A pinhole (p75s) with diameter $d = 75$ μm was placed in the beam path to shape the incident beam, and the resultant beam was illuminated on the digital micro-mirror device (DLP7000) to produce the 4096 speckles (64×64 pixels). Hence, the light field from the light source can be expressed as

$$E(\boldsymbol{x}_2) = \int E(\boldsymbol{x}_1) h(\boldsymbol{x}_1, \boldsymbol{x}_2)\, \mathrm{e}^{\frac{-\mathrm{i}k|\boldsymbol{x}_2|^2}{2f_1}} R(\boldsymbol{x}_2)\, \mathrm{d}\boldsymbol{x}_1, \qquad (1)$$

where $E(\boldsymbol{x}_1)$ is the light field from the laser, $h(\boldsymbol{x}_1, \boldsymbol{x}_2)$ is the impulse response function from the source to DMD, $\mathrm{e}^{\frac{-\mathrm{i}k|\boldsymbol{x}_2|^2}{2f_1}}$ denotes the transmission function of the len L_1 ($f = 50$ mm), $R(\boldsymbol{x}_2)$ denotes the speckle pattern matrices transmitted from the DMD. In the experiment, a set of Hadamard speckle pattern pairs with 64×64 pixels were prepared, and then loaded on the DMD in sequence to produce the speckles.

The calibration unit, consisted of len L_2 ($f = 100$ mm), a diaphragm ($d = 50$ mm), and a Dove prism, was used to adjust the speckles. There were multiple diffraction orders in the beam from the DMD. The len L_2 was used to concentrate the beam and the diaphragm was applied to select the first diffraction order. The Dove prism was used to rotate back the patterns since the DMD has rotated the beam by 45°. Thereafter, the beam was collimated by the beam expander unit, including len L_3 ($f = 50$ mm) and len L_4 ($f = 250$ mm). To simulate the un-

derwater environment, a 1 m×0.4 m×0.4 m tank with distilled water was placed on the path before the unknown object. The light field after the underwater environment can be expressed as

$$E(\boldsymbol{x}_3) = \int E(\boldsymbol{x}_2) h(\boldsymbol{x}_2, \boldsymbol{x}_3) \mathrm{e}^{\frac{-\mathrm{i}k|\boldsymbol{x}_3|^2}{2F}} \mathrm{e}^{\psi(\boldsymbol{x}_2, \boldsymbol{x}_3)} T(\boldsymbol{x}_3) \mathrm{d}\boldsymbol{x}_2, \quad (2)$$

where $h(\boldsymbol{x}_2, \boldsymbol{x}_3)$ is the impulse response function from the DMD to the object, $\mathrm{e}^{\frac{-\mathrm{i}k|\boldsymbol{x}_2|^2}{2F}}$ denotes the transmission function of the lens with equivalent focal F, $\mathrm{e}^{\psi(\boldsymbol{x}_2,\boldsymbol{x}_3)} = \mathrm{e}^{\alpha(\boldsymbol{x}_2,\boldsymbol{x}_3)+\mathrm{i}\beta(\boldsymbol{x}_2,\boldsymbol{x}_3)}$ is a complex-valued random process that denotes the effects of underwater environment, $\alpha(\boldsymbol{x}_2, \boldsymbol{x}_3)$ is the amplitude fluctuations while $\beta(\boldsymbol{x}_2, \boldsymbol{x}_3)$ is the phase fluctuations, and $T(\boldsymbol{x}_3)$ is the transfer function of the unknown object behind the tank.

Finally, the intensity $I(\boldsymbol{x}_4)$ was detected by the bucket detector (PMM02) ($\lambda = 280$–850 nm) in sequence, and recorded by the digitizer. The light field and its intensity are expressed as

$$\begin{aligned} E(\boldsymbol{x}_4) &= \int E(\boldsymbol{x}_3) h(\boldsymbol{x}_3, \boldsymbol{x}_4) \mathrm{e}^{\frac{-\mathrm{i}k|\boldsymbol{x}_4|^2}{2f_5}} \mathrm{d}\boldsymbol{x}_3, \\ I(\boldsymbol{x}_4) &= |E(\boldsymbol{x}_4)|^2. \end{aligned} \quad (3)$$

With the Hadamard speckle patterns, the object image can be reconstructed by the second-order correlation function, which can be expressed as

$$\begin{aligned} G(\boldsymbol{x}_2, \boldsymbol{x}_4) \;=\; & \langle R(\boldsymbol{x}_2) R^*(\boldsymbol{x}_2') E(\boldsymbol{x}_4) E^*(\boldsymbol{x}_4') \rangle \\ & - \langle R(\boldsymbol{x}_2) R^*(\boldsymbol{x}_2') \rangle \langle E(\boldsymbol{x}_4) E^*(\boldsymbol{x}_4') \rangle. \end{aligned} \quad (4)$$

The above equation can be rewritten as

$$\begin{aligned} & G(\boldsymbol{x}_2, \boldsymbol{x}_4) \\ = & \int \mathrm{d}\boldsymbol{x}_1 \mathrm{d}\boldsymbol{x}_1' \mathrm{d}\boldsymbol{x}_2 \mathrm{d}\boldsymbol{x}_2' \langle R(\boldsymbol{x}_2) E^*(\boldsymbol{x}_1') \rangle \\ & \times \langle E(\boldsymbol{x}_1) R^*(\boldsymbol{x}_2') \rangle h(\boldsymbol{x}_1, \boldsymbol{x}_2) h^*(\boldsymbol{x}_1, \boldsymbol{x}_2') \\ & \times h(\boldsymbol{x}_2, \boldsymbol{x}_3) h^*(\boldsymbol{x}_2, \boldsymbol{x}_3') h(\boldsymbol{x}_3, \boldsymbol{x}_4) h^*(\boldsymbol{x}_3, \boldsymbol{x}_4') \\ & \times \mathrm{e}^{\frac{-\mathrm{i}k|\boldsymbol{x}_2|^2}{2f_1}} \mathrm{e}^{\frac{\mathrm{i}k|\boldsymbol{x}_2'|^2}{2f_1}} \mathrm{e}^{\frac{-\mathrm{i}k|\boldsymbol{x}_3|^2}{2F}} \mathrm{e}^{\frac{\mathrm{i}k|\boldsymbol{x}_3'|^2}{2F}} \mathrm{e}^{\frac{-\mathrm{i}k|\boldsymbol{x}_4|^2}{2f_5}} \\ & \times \mathrm{e}^{\frac{\mathrm{i}k|\boldsymbol{x}_4'|^2}{2f_5}} \langle \mathrm{e}^{\psi(\boldsymbol{x}_2,\boldsymbol{x}_3)+\psi^*(\boldsymbol{x}_2,\boldsymbol{x}_3')} \rangle T(\boldsymbol{x}_3) T(\boldsymbol{x}_3'). \end{aligned} \quad (5)$$

Note that the bucket detector should be replaced by a power sensor (S120C) when the power is detected.

To demonstrate the result of the CGI, the structural similarity image measurement (SSIM) was used to measure the image quality, which is combined with three comparisons: luminance, contrast, and structure. The luminance comparison can be expressed as

$$\ell(X, Y) = \frac{2u_x u_y + C_1}{u_x^2 + u_y^2 + C_1}, \quad (6)$$

where X is the original image and Y is the reconstructed image, u_x and u_y are the means of X and Y , respectively, C_1 is the constant to avoid instability when $u_x^2 + u_y^2$ is very close to zero. Specifically, C_1 is assumed to be

$$C_1 = (K_1 L)^2, \quad (7)$$

where L is the dynamic range of the pixel values, and $K_1 \ll 1$ is a small constant.

The contrast comparison is defined as

$$c(X, Y) = \frac{2\sigma_x \sigma_y + C_2}{\sigma_x^2 + \sigma_y^2 + C_2}, \quad (8)$$

where σ_x^2 and σ_y^2 are the standard deviations of X and Y, respectively, $C_2 = (K_2 L)^2$, and $K_2 \ll 1$ is a small constant.

The structure comparison is defined as

$$s(X, Y) = \frac{\sigma_{xy} + C_3}{\sigma_x \sigma_y + C_3}, \quad (9)$$

where σ_{xy} can be estimated as

$$\sigma_{xy} = \frac{1}{N-1} \sum_{i=1}^{N} (X_i - u_x)(Y_i - u_y). \quad (10)$$

Finally, the SSIM index between images X and Y is given by

$$\mathrm{SSIM}(X, Y) = [\ell(X, Y)]^\alpha [c(X, Y)]^\beta [s(X, Y)]^\gamma, \quad (11)$$

where α, β, $\gamma > 0$ are parameters used to adjust the relative importance of the three components. With $\alpha = \beta = \gamma = 1$ and $C_3 = C_2/2$, the SSIM index has a specific form

$$\mathrm{SSIM}(X, Y) = \frac{(2u_x u_y + C_1)(2\sigma_x \sigma_y + C_2)}{(u_x^2 + u_y^2 + C_1)(\sigma_x^2 + \sigma_y^2 + C_2)}. \quad (12)$$

The value of SSIM is between 0 and 1, and a higher value indicates a higher similarity.

3. Experimental demonstrations and discussion

In this section, we investigate the quality of underwater GI for the unknown object (64×64 pixels) influenced by the temperature gradient, water vibration, and turbid medium. The influence of temperature gradient on the underwater GI is presented in Subsection 3.1, the effect of vibration on the underwater GI is given in Subsection 3.2, and the discussion about turbid medium $CaCO_3$ on the underwater GI is introduced in Subsection 3.3.

3.1. Influence of temperature gradient on underwater GI

Since the heater used in the experiment is a point-heating, the effect caused by the temperature gradient on the propagating beam may be different when the heater is located at different positions of the tank. Hence, we set up four different positions of the tank to produce the temperature fluctuations in the experiment, which are labeled as A, B, C, and D in Fig. 1. The height of water is 10 cm, and the optical path is 4.5 cm below the water surface. The heater is used to heat the water near

the surface. A thermometer is used to measure the temperature of the bottom and surface of water respectively. Thus, the gradient of temperature can be obtained by computing the temperature difference between the bottom and surface of water. To verify that heating water at different locations could have different results, we chose four positions (positions *A* and *D* are at the end of the underwater optical path, and positions *B* and *C* are at the front of the underwater optical path. All the positions are exactly symmetrical against the beam path) to set up the thermometer.

Figure 2 shows the results of underwater computational GI under different temperature gradients, where the influence of temperature gradients at different positions is presented, and the temperature gradient is controlled from 0 °C to 5.5 °C. A rabbit doll was used as the unknown object. The results show that the underwater ghost imaging is slightly affected by the temperature gradient, and there are no apparent differences among the images reconstructed under different temperature gradients. There is some distortion of the images when the temperature gradient is greater than 5.0 °C. At the same time, the temperature gradient produced at different positions (*A*, *B*, *C*, and *D*) almost has no influence on the reconstructed images.

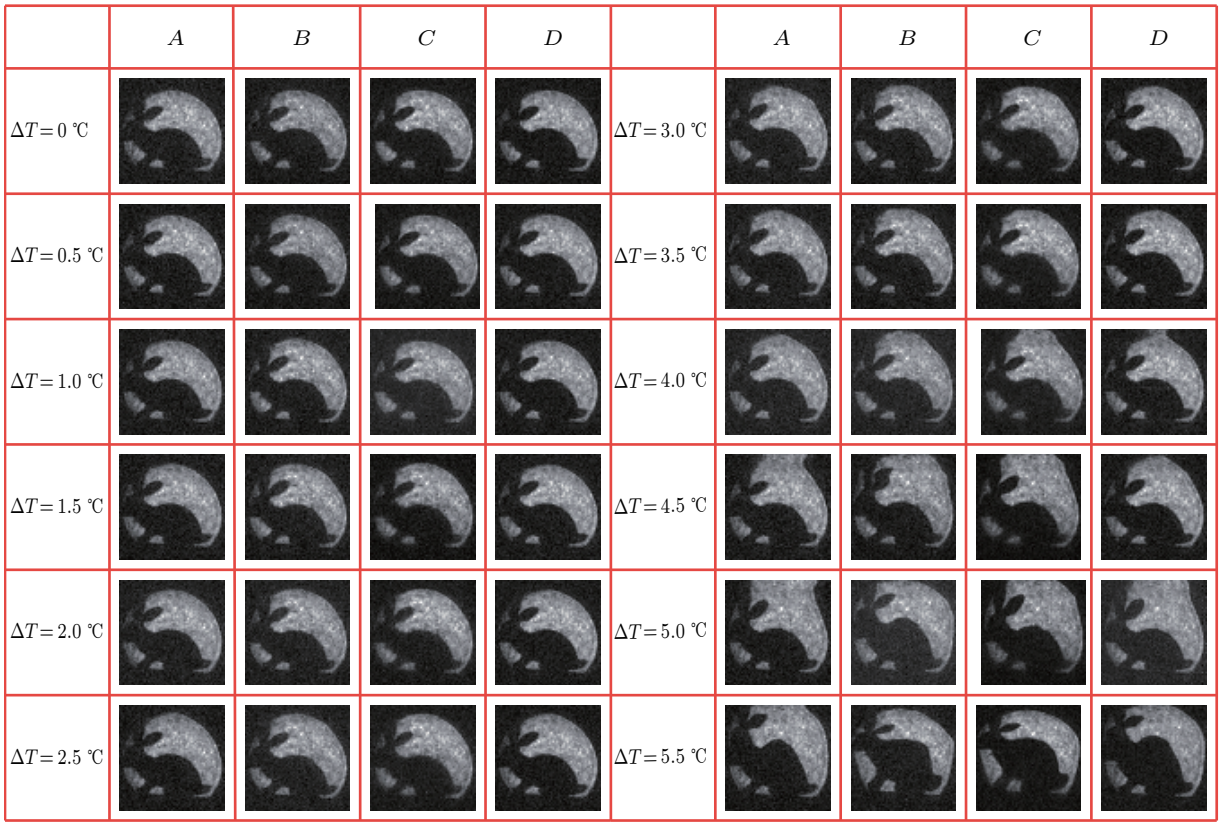


Fig. 2. The experimental results of underwater computational GI under different temperature gradients, where the influence of temperature gradients at different positions (*A*, *B*, *C*, and *D*) is presented, and the temperature gradient is controlled from 0 °C to 5.5 °C.

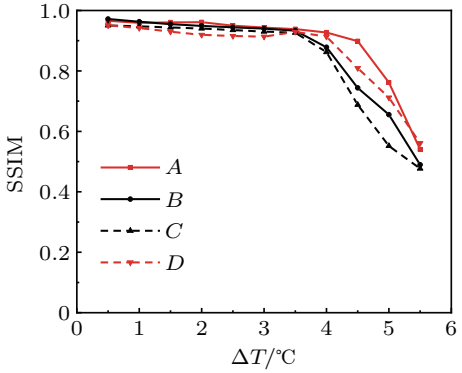


Fig. 3. The SSIM values of the reconstructed image against the temperature gradients.

To further analyze the influence of the temperature gradient on the underwater GI, we present the SSIM values of the reconstructed image against the temperature gradients at positions *A*, *B*, *C*, and *D* in Fig. 3.

The experimental results show that the quality of the recovery image from the underwater computational GI system has little change when the temperature gradient is lower than 4.0 °C, which might be corresponding to the weak oceanic turbulence, and the SSIM values degrade when the temperature gradient is higher than 4.0 °C. However, the SSIM values are still higher than 0.47683, which means that the underwater computational GI is well reconstructed even though the temperature gradient is greater than 4.0 °C. The results also show that the degradations at positions *B* and *C* are faster than those at positions *A* and *D*, which indicates that the influence of

the temperature gradient on the underwater computational GI is different when the temperature gradient is produced at the front or at the end of the optical path. Furthermore, the SSIM values at positions A and D, B and C are almost the same, which indicates that the two sides with the same distance to the beam path have the similar influence on the underwater computational GI system.

3.2. Influence of vibration on underwater GI

The propagation of the light beam would be misaligned when the water vibration occurs in the underwater environment, since the light is absorbed and scattered. So we discuss whether or not the water vibration affects the quality of underwater computational GI. Here, the water vibration is caused by a heavy force on the tank at some frequency. We use the water plane with no waves for the reference, and record the height of the wave as 0 cm. Then, by the heavy force on the tank, different vertical heights of wave are measured. The wave vibration in the experiment is from 0 cm to 5 cm. Figure 4 shows the SSIM values of the reconstructed image from underwater computational GI against the water vibration.

As seen from Fig. 4, the SSIM values change very little when the wave vibration is from 0 cm to 5 cm, and all the SSIM values are greater than 0.9. It indicates that the computational GI system is disturbance-free from the wave vibration.

L/cm	0	1	2	3	4	5
SSIM		0.970191	0.968395	0.96773	0.964837	0.94346

Fig. 4. The reconstructed target images with different wave heights, where SSIM is presented together.

3.3. Influence of turbid medium $CaCO_3$ on underwater GI

Since the wavefront of light would be distorted and may be multiple scattered when the beam passes through the turbid medium. We further study the influence of turbid media on the underwater computational GI by adding some $CaCO_3$ in the tank water. To describe the turbidity caused by $CaCO_3$, we use the ratio between weight of $CaCO_3$ and that dc of the tank water, and the turbidity can be expressed as

$$T = \frac{M_{\mathrm{CaCO_3}}}{M_{\mathrm{water}}}. \tag{13}$$

As shown in Fig. 1, we added different weights of $CaCO_3$ in the distilled water to generate different turbidities. We added 50 mg $CaCO_3$ in the distilled at each time, and one image was reconstructed at the corresponding turbidity. The mass of $CaCO_3$ was from 50 mg to 1000 mg in the experiment, meanwhile the turbidity was from 1.25×10^{-6} to 2.5×10^{-5}. To show the power attenuation as the light beam passing through the turbid water, the power attenuation against the different mass of the turbid medium is shown in Fig. 5(a), where the power was measured by an optical power meter, and the SSIM values of the reconstructed images from underwater computational GI against the turbidities are shown in Fig. 5(b). Figure 5(a) shows that the power and the intensity of the light beam are attenuated when the turbidity increases. Figure 5(b) shows that the SSIM values degrade when the turbidity increases. However, the SSIM value of the reconstructed image is still higher than 0.5 when the mass of $CaCO_3$ is 1000 mg and the turbidity is 2.5×10^{-5}, where the tank water is fully opaque. It is shown that the underwater computational GI has the deblur ability with turbid media.

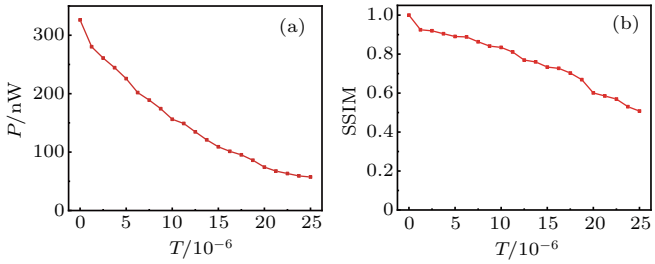


Fig. 5. (a) The power attenuation of light and (b) SSIM changes of GI through the water with turbidity from 1.25×10^{-6} to 2.5×10^{-5}.

4. Conclusion

We have experimentally demonstrated the ability of computational GI in underwater environment, and investigated the influence of temperature gradient, water vibration, and turbid media on the quality of the reconstructed image from the computational GI system. The results show that the underwater GI has an anti-underwater turbulent imaging ability. The quality of the reconstructed image from underwater computational GI decreases slightly with the low temperature gradient, wave vibration, and turbid media. Only when the temperature gradient is greater than 4.0 °C, the SSIM value starts to decrease significantly. Additionally, the same temperature gradient produced at different portions has slight effect on the quality of the underwater GI. The turbulence-free ability of computational GI

has hinted that the computational GI would have a well imaging ability in the long underwater environment.

References

[1] Sun C D, Chen L Y, Gao L M, Zhang J S and Di L 2000 *J. Appl. Opt.* **4** 39
[2] Hou W L 2009 *Opt. Lett.* **34** 2688
[3] McGlamery B L 1976 *J. Opt. Soc. Am.* **66** 174
[4] Hou W L, Woods S, Jarosz E, Goode W and Weidemann A 2012 *Appl. Opt.* **51** 2678
[5] Padgett M J and Boyd R W 2017 *Philos. Trans. R. Soc. A* **375** 20160233
[6] Shapiro J H and Boyd R W 2012 *Quantum Inf. Process.* **11** 949
[7] Pittman T B, Shih Y H, Strekalov D V and Sergienko A V 1995 *Phys. Rev. A* **52** R3429
[8] Bennink R S, Bentley S J and Boyd R W 2002 *Phys. Rev. Lett.* **89** 113601
[9] Shapiro J H 2008 *Phys. Rev. A* **78** 061802
[10] Wang L, Zhao S M, Cheng W W, Gong L Y and Chen H W 2016 *Opt. Commun.* **366** 314
[11] Ferri F, Magatti D, Lugiato L A and Gatti A 2010 *Phys. Rev. Lett.* **104** 253603
[12] Sun B Q, Welsh S S, Edgar M P, Shapiro J H and Padgett M J 2012 *Opt. Express* **20** 16892
[13] Zhao S M and Zhuang P 2014 *Chin. Phys. B* **23** 054203
[14] Li M F, Zhang Y R, Liu X F, Yao X R, Luo K H, Fan H and Wu L A 2013 *Appl. Phys. Lett.* **103** 211119
[15] Bai X, Li Y Q and Zhao S M 2013 *Acta Phys. Sin.* **62** 44209 (in Chinese)
[16] Zhang Z B, Ma X and Zhong J G 2015 *Nat. Commun.* **6** 6225
[17] Zhao S M, Wang L, Liang W Q, Cheng W W and Gong L Y 2015 *Opt. Commun.* **353** 90
[18] Yu W K, Li M F, Yao X R, Liu X F, Wu L A and Zhai G J 2014 *Opt. Express* **22** 7133
[19] Zhu Y C, Shi J H, Yang Y and Zeng G H 2015 *Appl. Opt.* **54** 1279
[20] Bian L H, Suo J L, Hu X M, Chen F and Dai Q H 2016 *J. Opt.* **18** 085704
[21] Wang L and Zhao S M 2016 *Photon. Res.* **4** 240
[22] Bai Y F and Han S S 2007 *Phys. Rev. A* **76** 043828
[23] Zhao C Q, Gong W L, Chen M L, Li E R, Wang H, Xu W D and Han S S 2012 *Appl. Phys. Lett.* **101** 141123
[24] Li H G, Zhang Y T, Cao D Z, Xiong J and Wang K G 2008 *Chin. Phys. B* **17** 4510
[25] Luo B, Wu G H and Yin L F 2018 *Chin. Phys. B* **27** 094202
[26] Li H X, Bai Y F, Shi X H, Nan S Q, Qu L J, Shen Q and Fu X Q 2017 *Chin. Phys. B* **26** 104204
[27] Zhao S M, Yang H, Li Y Q, Cao F, Sheng Y B, Cheng W W and Gong L Y 2013 *Opt. Commun.* **294** 223
[28] Zhao S M, Wang B, Gong L Y, Sheng Y B, Cheng W W, Dong X L and Zheng B Y 2013 *J. Lightw. Technol.* **31** 2823
[29] Xiang Q, Yang K C, Yu L, Xia M, Li W and Guo W P 2015 *Acta Opt. Sin.* **35** 0711002
[30] Gao Y, Fu X Q and Bai Y F 2017 *J. Opt.* **46** 410
[31] Le M N, Wang G, Zheng H B, Liu J B, Zhou Y and Xu Z 2017 *Opt. Express* **25** 22859
[32] Zhang Q W, Li W D, Liu K, Zhou L W, Wang Z M and Gu Y J 2019 *J. Opt. Soc. Am. A* **36** 397
[33] Luo C L, Li Z L, Xu J H and Liu Z M 2018 *Laser Phys. Lett.* **15** 125205
[34] Zhang Y, Li W D, Wu H Z, Chen Y H, Su X Y, Xiao Y, Wang Z M and Gu Y J 2019 *Opt. Commun.* **441** 45